Chapter 2

Background and Papers Reviews

This chapter introduces some background and papers reviews relevant to the discussions in this dissertation. Section 2-1 is a summary of the magnetoresistance effects; include the pseudo-spin-valve (PSV) effect and the tunneling magnetoresistance (TMR) effect. In the Section 2-2, some characters of exchange anisotropy and some common metallic FM/AFM exchanged biased systems will be discussed. Then, the thermal degenerations and some improvements of the magnetic random access memory (MRAM) cells are described in the section 2-3. Finally, the section 2-4 will present the general properties and some experimental results of Os.

2-1 Magnetoresistance effects

In this section, the magnetoresistance, including the pseudo spin valve effect and the tunneling magnetoresistance effect, will be discussed.

2-1-1 Pseudo-Spin-Valve effect

Spin-valves are composed of a free and a pinned layer separated by a nonmagnetic layer. The spin valve structure allows low-field giant magnetoresistance (GMR) effect and has some applications in magnetic read heads [16-18]. The MR properties of the two types of spin-valves are different, spin valves having an antiferromagnetic pinned layer with exchange-biased field and pseudo-spin-valves having only a hard magnetic layer [19]. The pseudo-spin-valve is composed a hard magnetic (HM) layer, and a soft magnetic (SM) one,

magnetically separated by a nonmagnetic (NM) layer. The HM has a larger coercivity field (H_c) than the SM. A prototype pseudo-spin-valve film proposed by Shinjo et al. is [NiFe (3)/Cu (5)/Co (3)/Cu (5)]^{15} multilayered film [20]. Here, NiFe is used for the SM and Co acted as the HM. This multilayered film showed a MR ratio of ~ 8 %. The magnetocrystalline anisotropy energy, E_a, for the films having cubic symmetry is given as

$$E_a = K_1/8(1-\cos 4\theta)+\cdots \quad (1)$$

when the magnetization rotates in the (100) plane, where θ is the angle between the magnetization direction and the [010] axis. The K_1 is the negative for face center cubic (fcc) NiFe and Co. Therefore, the NiFe and Co layers have an easy axis along the [010] direction. This is the reason why the magnetization reversal of the NiFe and Co layers takes place. These characteristics are suitable for the application of pseudo-spin-valves to MRAM devices. As the magnetization reversal of the HM (i.e. Co) layers is used for data writing and that of SM (i.e. NiFe) layers is used for data reading, the switching field of SM layers is lower than that of the HM layers. The schematic magnetization curve and the MR curve of the pseudo-spin-valve are shown in Fig. 2-1 (a) and (b). With the application of a small magnetic field that causes magnetization reversal of the HM, the magnetization directions of the SM and HM take a parallel configuration and the pseudo-spin-valve shows low resistance. Especially in recent years, many possible applications have been proposed in magnetoresistive sensors, in read heads for hard disks and in tape magnetic data storage. Due to their intrinsic properties, spin valve devices will allow the realization of sensitivities which are up to an order of magnitude higher [21-24] than those obtained in heads based on (conventional) Anisotropic Magneto-Resistance (AMR) materials. Later on, its application in MRAM was also proposed and lately many achievements have been reported [25-30].

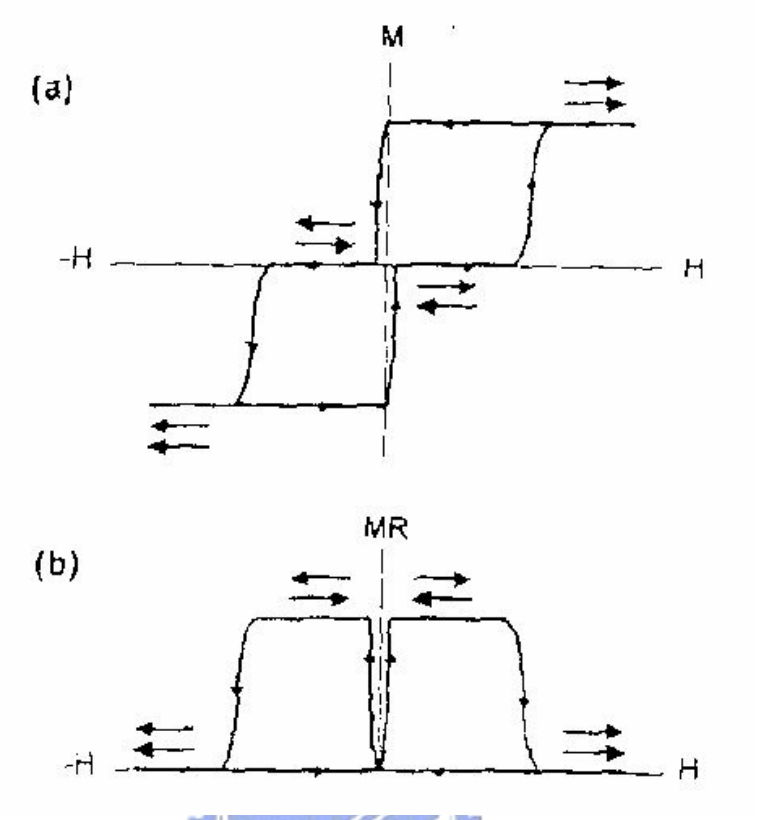

Fig. 2-1 (a) Magnetization curve and (b) MR curve of the pseudo-spin-valve, where the magnetization directions of the SM and HM are denoted with different arrows. (Data are from Ref. [140])

2-1-2 Tunneling magnetoresistance effect

TMR is observed for ferromagnetic spin tunneling junction (MTJ) consisting of ferromagnetic-insulator-ferromagnetic layers [31-33]. When the insulating layer, usually referred to as the barrier layer, is very thin (on the order of 1 nm), electrons can tunnel through this forbidden region as a result of the wave-like nature of electrons due to a voltage applied between the two electrodes, a phenomenon which can only be described in terms of quantum mechanics. The basic principle of TMR is the dependence of the tunneling

probability on the relative orientation of magnetization in the two ferromagnetic electrodes. The tunneling conductance is spin dependent due to the spin dependent density of states (DOS) at the Fermi level for ferromagnets. When the applied voltage is small enough for electrons near the Fermi level to tunnel, the tunneling conductance, G, in the MTJ can be written as (2)-(4) by neglecting the spin dependency of the tunneling probability [34],

$$G = R^{-1} = \sum_{\sigma} |T|^2 D_{1\sigma}(E_F) D_{2\sigma}(E_F) \quad (2)$$

$$|T|^2 = \exp(-2s\chi) \quad (3)$$

$$\chi = \left[8\pi^2 m \times (\varphi - E_F)/h^2\right] \quad (4)$$

where R, T, and $D_{i\sigma}(E_F)$ are the junction resistance, tunneling probability, and DOS at the Fermi level for spin σ band of the i-th ferromagnet, respectively, and φ, s, χ, and h are the barrier height and thickness, electron wave vector in the barrier and the Planck constant, respectively. The TMR is defined as

$$TMR = (R_{AP}-R_P) / R_P \quad (5)$$

where R_P and R_{AP} are the resistance for parallel and antiparallel spin configurations of two ferromagnetic electrodes, respectively. If we assume that spin is conserved during tunneling as shown in Fig. 2-2, (2)-(5) lead to Julliere's model [31],

$$TMR = 2P_1P_2 / (1-P_1P_2) \quad (6)$$

Pi is the spin polarization of tunneling electrons of ferromagnet i and given by

$$P_i = (D_{i\uparrow}-D_{i\downarrow}) / (D_{i\uparrow}+D_{i\downarrow}) \quad (7)$$

TMR can vary over a wide range depending on the P values of ferromagnets as verfied by (6) and (7). For vanishing polarization of one of the electrodes the magnetoresistance disappears, while for full polarization of the tunneling electrons of both electrodes (P_1=P_2=1) the effect will become infinitely large corresponding to a value of 1 in (6). Unfortunately, determining the spin polarization at the Fermi energy of a ferromegnet is not easy. A typical transition metal ferromagnet has two components to broad s-band with a lesser degree of spin polarization due to hybridization with the d-bonds. The value of P is controlled by extending by the amount to which these s- and d-bonds cross the Fermi energy. If the orbital character at the Fermi surface of the ferromagnetic metal is primarily d-like, then the spin polarization will be high. If the orbital character, however, is s-like or s-d hybridized, then the spin polarization can be low or high depending on the details of the electronic structure. The magnetization of a material may show that all the electronic spins associated with the d orbits are aligned, but the spin polarization at E_F can be depressed. On the other hand, metallic oxide ferromagnet, for example, have a greater opportunity for high spin polarization because of the predominance of the d orbital character at E_F.

The values of P measured are shown in Table 2.1 for various ferromagnets, except for the theoretically expected values for half metals with P = 1, which have an energy gap in the minority spin (down spin) band as shown schematically in Fig. 2-3; thus only majority spin (up spin) electrons are at the Fermi level. The spin polarization of tunneling electrons seems to be nearly proportional to the magnetic moment μ of the electrode, as shown for NiFe alloys in Fig. 2-4 [35], while it is not always proportional to μ of the ferromagtic electrode, as shown in Fig. 2-5 [36], which exhibits TMR and μ^2 as a function of the composition of CoFe alloy electrodes used for the junctions.

Table 2.1 Spin polarization of various magnetic materials (Data are from Ref. [140])

Magnetic material	Spin polarization	Magnetic material	Spin polarization
Fe	0.44	Co	0.35
Ni	0.23	$Ni_{80}Fe_{20}$	0.25, 0.45
$Fe_{50}Co_{50}$	0.53	NiMnSb	1, 0.58
PtMnSb	1	CrO_2	1
Fe_3O_4	1	(La-Sr)MnO_3	1

Equation (6) assumes that all electrons at the Fermi level have the same probability of tunneling and also neglects the influence of the barrier. In fact, however, TMR depends on tunneling barrier height for the MTJ using CoFe electrodes. The TMR is larger for the higher barrier height. The barrier height can be estimated by Simmon's expressions (8)-(11) [37]

$$J = \beta\left(V + V^3\right) \tag{8}$$

$$\beta = \left[3e^2\left(2m\phi\right)^{1/2}/2h^2 s\right]\exp\left(-A\phi^{1/2}\right)\left[\Omega^{-1}cm^2\right] \tag{9}$$

$$\gamma = \left(Ae^2\right)/96\phi - Ae^2/32\phi^{1/4} \tag{10}$$

$$A = 4\pi\left(2m\right)^{1/2} s/h = 1.02\left[A/\left(eV\right)^{1/2}\right] \tag{11}$$

for lower bias voltage, where J, φ, and s are current density [A/cm^2], barrier height [eV], and barrier thickness [cm], respectively. For junctions with large tunneling barrier height, the model well explains the experimental results of TMR, which exhibits experimental TMR as a function of $2P_1P_2/(1-P_1P_2)$ for various junctions with different magnetic electrodes, where the experimentally obtained P was used. However, there is a serious failure in Julliere's model; that is, the sign of the spin polarization is different from experiments. The tunneling

experiments of Tedrow and Meservey exhibited positive spin polarization for all the analyzed transition metals [38], in contrast with experiments. In transition metals like Co or Ni, a negative spin polarization is expected because their 3d-band is negatively polarized at the Fermi level. To explain these results, it has been claimed, for instance, that only some itinerant d electrons tunnel or that only the s electrons, with lower DOS but positive spin polarization, can tunnel. All these explanations are unsatisfactory, and the results of Tedrow and Meservey have remained a mystery for more than 20 years. Recently, however, Teresa et al. [39], demonstrated in experiments with junctions consisting of ferromagnetic trasition metal/insulator/half metal that the sign of the spin polarization depends of the barrier materials, and that selection by the barrier of the character of the tunneling electrons can be explained by the character of the bonding between the electrode and the barrier.

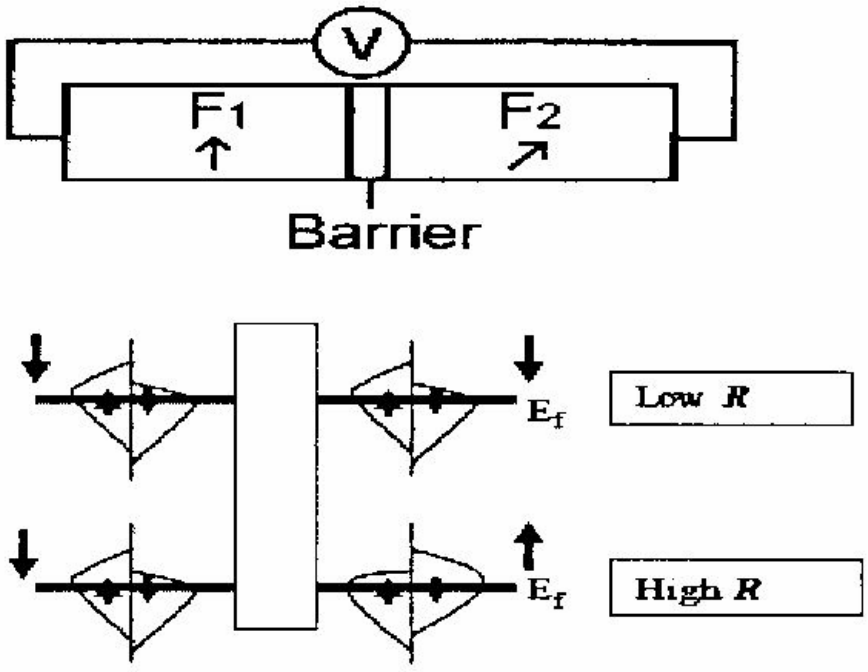

Fig. 2-2 Schematic model for spin dependent tunneling. (Data are from Ref. [140])

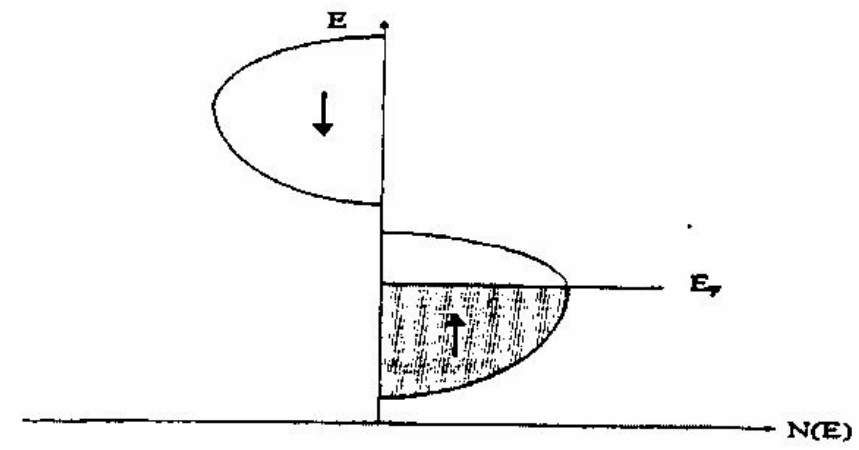

Fig. 2-3 Schematic energy band structure for a half metal. (Data are from Ref. [140])

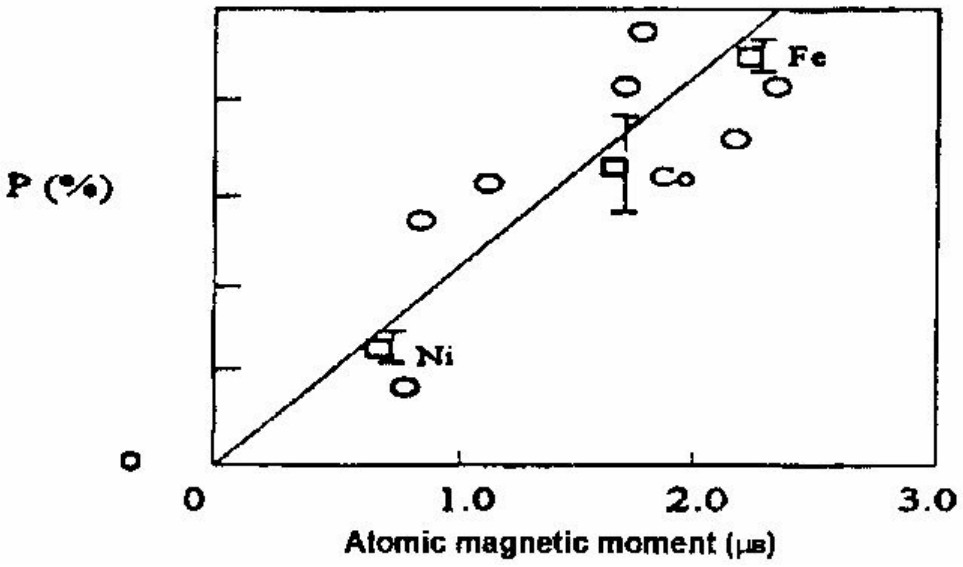

Fig. 2-4 Spin polarization of tunneling electrons vs. the magnetic moment μ of the electrode. (Data are from Ref. [141])

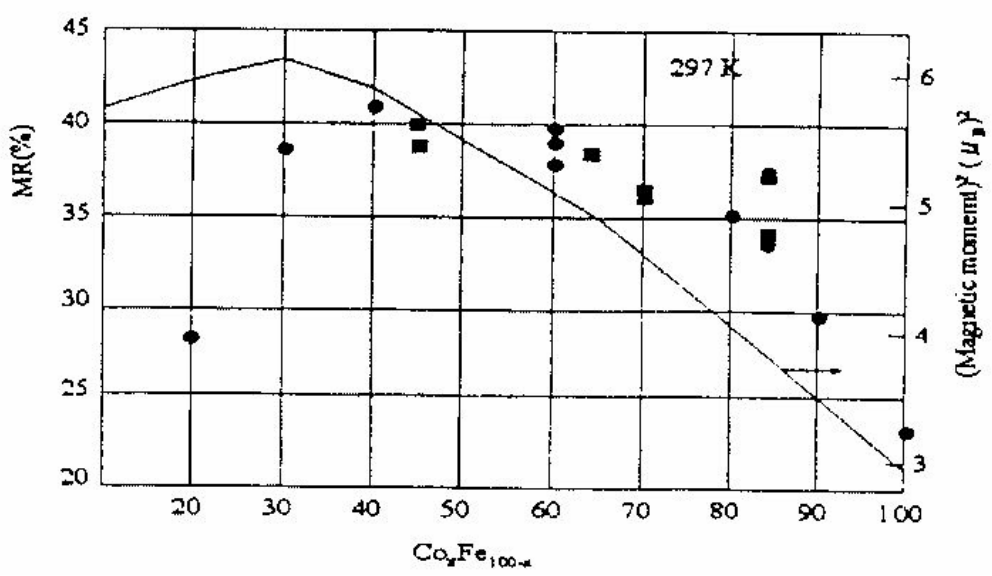

Fig. 2-5 TMR and μ^2 as function of the composition of Fe-Co alloy electrodes used for the junctions. (Data are from Ref. [141])

2-2 Metallic FM/AFM exchanged biased systems

The term exchange anisotropy was used to describe a magnetic interaction between a ferromagnet (FM) and an antiferromagnet (AFM). Since the first experiments of Meiklejohn and Bean [40], many FM/AFM systems have been explored to increase the scientific understanding of them. In addition to symmetry breaking related to the appearance of the unidirectional anisotropy that brings about the exchange field (H_{ex}), several supplementary remarkable features are associated with exchange anisotropy. First is the existence of a critical temperature called blocking temperature, T_B, above which exchange anisotropy vanishes. Usually T_B can be considerably lower than the Néel temperature (T_N) of coupled ferromagnet. Another remarkable feature of exchange anisotropy is the training effect, i.e. the dependence of exchange field on the number of measurements n, with the value of H_{ex} decreasing as n increases [41], which constitutes a hint that the interface actually is in metastable equilibrium. An important feature: the memory effect, which consists of the fact that the system keeps a memory of the temperature at which it was field-cooled [42]. Furthermore, another characteristic associated with many exchange anisotropy systems, observed at $T < T_B$, is a large increase of the coercivity. The memory effect was widely used in the memory and head devices in the recent years. Due to the device performance is very depending on thermal treatment. Too high temperature during manufacturing process will cause thermal degrading, and one of the factors to examine the thermal stability is what temperature the H_{ex} can keep the similar amplitude of its maximum value.

However, exchange anisotropy was not of interest to industry until Hempstead et al. [43] proposed that unidirectional exchange anisotropy between NiFe and FeMn could be useful for biasing small magnetresistive sensors and also for suppressing Barkhausen noise. Almost all of the current applications of exchange anisotropy for film biasing use metallic AFMs. The

crystal structures of metallic AFMs often deviate more strongly from cubic symmetry than do the structures of the insulating AFMs. This makes it more difficult to grow suitable epitaxial films, whether bilayer or multilayer. The spin structures are generally more complex in metallic AFM: i.e. multi-spin sublattices, as well as temperature-dependent spin phases. The T_Ns of the metallic AFMs are usually higher than for insulating AFMs. There are some well-used FM/AFM systems will be discussed as following.

2-2-1 Fe-Mn

AFM Fe-Mn films with various additions are current in use in most exchange-biased MR read-heads. The AFM γ-phase is face center cubic (fcc), and extends from about 30-55 at% Mn at room temperature [44]; T_N increase from about 425-525 K with increasing Mn concentration in this range. Most investigations use alloy with 50% or more Mn to achieve the higher T_N (and, hence, T_B). The Mn and Fe atoms at the (0, 0, 0), (0, ½, ½), (½, 0, ½), and (½, ½, 0) form a tetrahedron, and the spins on these atoms are directed along the four <111> directions towards the center of this tetrahedron [44]. When fcc permalloy ($Ni_{81}Fe_{19}$) is the FM, lower H_c is achieved when the FeMn is deposited on the permalloy than when the deposition order is reversed, and the substrate is not fcc. A number of papers have interpreted the temperature dependence of H_{ex}, H_c, and T_N in terms of several interfacial issues, e.g., interfacial magnetic disorder [45], varieties of exchange paths [46], directional distributions of pinning fields due to the polycrystalline interface [47], or interfacial structure features [48-49]. These considerations are evidence of the growing recognition that detailed atomics scale magnetic and structural characterization of the FM-AFM interface is the key to understanding exchange anisotropy phenomena.

2-2-2 Ni-Mn

The search for higher T_B and a more corrosion-resistant AFM has led to the characterization of a number of other Mn-based alloys. The ordered face center tetragonal (fct) θ -phase of NiMn extends from ~43 to ~53 at% Mn [50]. The Mn atoms, with moments ≈ 3.8 μ_B, and the Ni atoms, with virtually no moment (< 0.2μ_B), are alternately placed on (002) planes [50-51]. The nearest-neighbor Mn atoms are coupled AFM, with the next-nearest-neighbors FM. At temperature > ~ 1050 K, the θ -phase transforms to a disordered body center cubic (bcc) phase, and the magnetic order disappears [50]. Lin et al. [52] compared H_{ex} and H_c of $Ni_{50}Mn_{50}$ and $Fe_{46}Mn_{54}$ bilayers with $Ni_{81}Fe_{19}$. After annealing at 240 and 255°C for 240 and 255 h, respectively, the bilayers with $Ni_{50}Mn_{50}$ had $\Delta\sigma$ values of 0.27 erg/cm^2, three times that of the $Fe_{46}Mn_{54}$ biased films. T_B was > 400°C for the $Ni_{50}Mn_{50}$ film, as compared to ~ 150°C for the $Fe_{46}Mn_{54}$ biased film. Corrosion resistance was also superior for the $Ni_{50}Mn_{50}$/ $Ni_{81}Fe_{19}$ bilayer. However, the annealing to produce the AFM fct phase increased H_c to 47 Oe, as compared to 5 Oe for the $Fe_{46}Mn_{54}$/ $Ni_{81}Fe_{19}$ bilayer.

2-2-3 Ir-Mn

In the disorder fcc γ-phase from ~ 10 to ~ 30 at% Mn, T_N increases from ~ 600 to ~ 750 K [53]. The average spins on each (002) plane are aligned parallel along the c-axis with alternating signs on neighboring (002) planes [53-54]. The average moments per atom are ~ 2.5 μ_B up to ~ 20 at% Mn, drop to 0.8 μ_B at ~ 25.6 at% Mn [55]. Fuke et al. [56] characterized spin valves in which $Ir_{20}Mn_{80}$ films were used to bias $Co_{90}Fe_{10}$ films. H_{ex} varied with the $Co_{90}Fe_{10}$ thickness, and $\Delta\sigma$ was 0.19 erg/cm^2 at room temperature for the as-deposited couples, and decreased to about 0.16 erg/cm^2 after annealing at 280°C for 5 min. in an applied field. $\Delta\sigma$ decreased monotonically with temperature, and T_B was ~ 265°C before and after the anneals. H_c for the as-deposited films was ≈ 100 Oe.

2-2-4 Pt-Mn

Chemically ordered Pt-Mn alloys are AFM with T_N ranging from 485 K for 66 at% Mn to a maximum value of 975 K at the equiatomic composition, decreasing to 815 K at 41 at% Mn [57-58]. Utilizing these high T_N values requires achieving the ordered structure in films. Farrow et al. [59] prepared a number of $Mn_xPt_{(1-x)}$ with permalloy using a variety of substrates and underlayers to encourage growth of an ordered structure. Their X-ray diffraction data were generally consistent with an ordered structure for films grown at 200°C. The best results were obtained on an MgO (001) substrate with an 18.6 nm $Mn_{56}Pt_{44}$ film. $\Delta\sigma$ was 0.032 erg/cm^2 at room temperature, and H_c was 19 Oe for the 10.9 nm permalloy film. $\Delta\sigma$ decreased monotonically from 77 K, and extrapolated values from MR data suggested a T_B > 500 K. However, heating the film to 180°C for the MR measurements decreased $\Delta\sigma$, possibly due to interdiffusion.

2-2-5 Other Mn-based AFM films

Ordered Mn_3Rh has a triangular spin arrangement below its T_N of 850 K. Velosa et al. [60] have investigated spin valves with $Mn_{78}Rh_{22}$ films biasing $Co_{90}Fe_{10}$. $\Delta\sigma$ was ≈ 0.19 erg/cm^2, and T_B was ~ 250 ℃. Besides, several ternary AFM Mn-based alloys have been examined. These include Pd-Pt-Mn [61-62], and Cr-Mn-Pt [63]. A particularly comprehensive comparison of the properties of FeMnRh, IrMn, RhMn, PdPtMn, NiMn, and CrPtMn, as seen from Table 2.2, has been reported by Lederman [64].

Table 2.2 Particularly comprehensive comparison of the properties of some metallic AFM materials (Data are from Ref. [64])

	NiFe	Cu	CoFe	FeMnRh	IrMn	RhMn	PdPtMn	NiMn	CrPtMn
Minimum Thickness (Å)				100	70	140	~250	~350	350
Annealing Temperature (°C)				175	175	175	~230	250-260	225
Blocking Temperature (°C)				150	190/230	~225	350	>425	300
Exchange Field (annealed) on Ta50/NiFe50Å (Oe)				300	270	306	230	390	160
Coercive Field (annealed) on Ta50/NiFe50Å (Oe)				40	40	109	110	180	32
Exchange Field on Cu200/CoFe50Å (Oe)				113.4	170	200			
Coercive Field on Cu200/CoFe50Å(Oe)				35	35	77			
Electrical Resistivity (μΩ.cm)	22	2	<12	210	325	200	185	210	360
Corrosion Potential (mV) (0.001M Na2SO4)	-105	-126	-575	-867	-930	-900	105	-815	-666
Icorrosion Density (μA)	0.005	0.037	0.34	11.5	11.9	30	0.15	3.75	1.72

2-3 Thermal degeneration of magnetic devices and improvements

Thermal treatment is an important issue for magnetic films. Due to the fabrications of magnetic devices include high-temperature process (standard CMOS process), annealing in a hydrogen atmosphere, plasma etching, insulating layer deposition, and so on. Many steps in this process flow will suffer the thermal degeneration problem. Previously reported thermal degeneration mechanisms in MTJs include: (1) The Mn diffusion from the AFM layer toward the tunnel barrier [65]; (2) Interdiffusion in the upper and lower electrodes [66]; and (3) Interdiffusion between the tunnel barrier and magnetic layers [67]. While the interdiffusion occurring, no matter the Mn atoms jumping into the FM layer or the tunneling layer, the electrode atoms entering into the FM layer, or the FM layer atomis diffusion into the tunneling layer, the breakdown of the FM layer appears. Thus, the coupling in the MTJs or other magnetic cells was disappeared. They will lose not only the magnetic behaviors but also electric properties. Many methods proposing to solve the problems listed above are introduced as following.

Many kinds of diffusion barrier were used to stop diffusion of the Mn atoms coming from the AFM layer. The reported barrier includes Ta [65, 68], CoFeOx [69-71], CoFeTaOx [72], MnCoFeO [73], AlOx [72], CoFePtx [74], FePtx [75], FeOx [76-77], FeN [78], Cr [79], and so on. They were posited between FM layer and AFM layer, FM layer and tunneling barrier layer, and in the center of the pined FM layer. Not only stopping the interdiffusion of Mn atoms but also increasing the magnetic and electrical properties was obtained by using such diffusion barrier materials. Although the actual reasons and mechanisms why they could stop the Mn atoms diffusion were still not clear, they really provide some solutions to make MTJ or other magnetic devices better thermal stability, shown in Fig. 2-6 and Fig. 2-7.

Except what mentioned above, other treatments of magnetic films were also used to enhance the thermal stability. The new Mn based alloys, such as PtMn [80], with high T_B were selected as the AFM layers. Thus, the magnetic films could bare higher annealing temperature without degeneration. The magnetic films with the synthetic AFM (SAF) structures, ex: Co/Ru/Co [81], CoFe/Ru/CoFe [82], CoFeB/Ru/CoFeB [83], and so on, were showed better thermal stability due to its stronger magnetic coupling. The special treatments of tunneling barrier, doping Fe [84] and Ti [85], also resulted in better performances of MTJs. Rapid Thermal annealing (RTA) was also performed to improve the quality of tunneling barrier [86-87], than the magnetic devices with higher performances and better thermal stability were obtained. Recent years, the amorphous FM material was used to raise the MR ratio of MTJs [88], and the MTJ with the combination structure of amorphous CoFeB (acts as FM layer) and crystal MgO (new type tunneling barrier) also showed the highest MR ratio [8] and the obvious thermal stability.

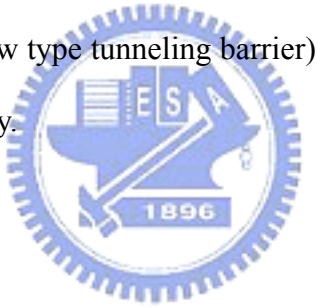

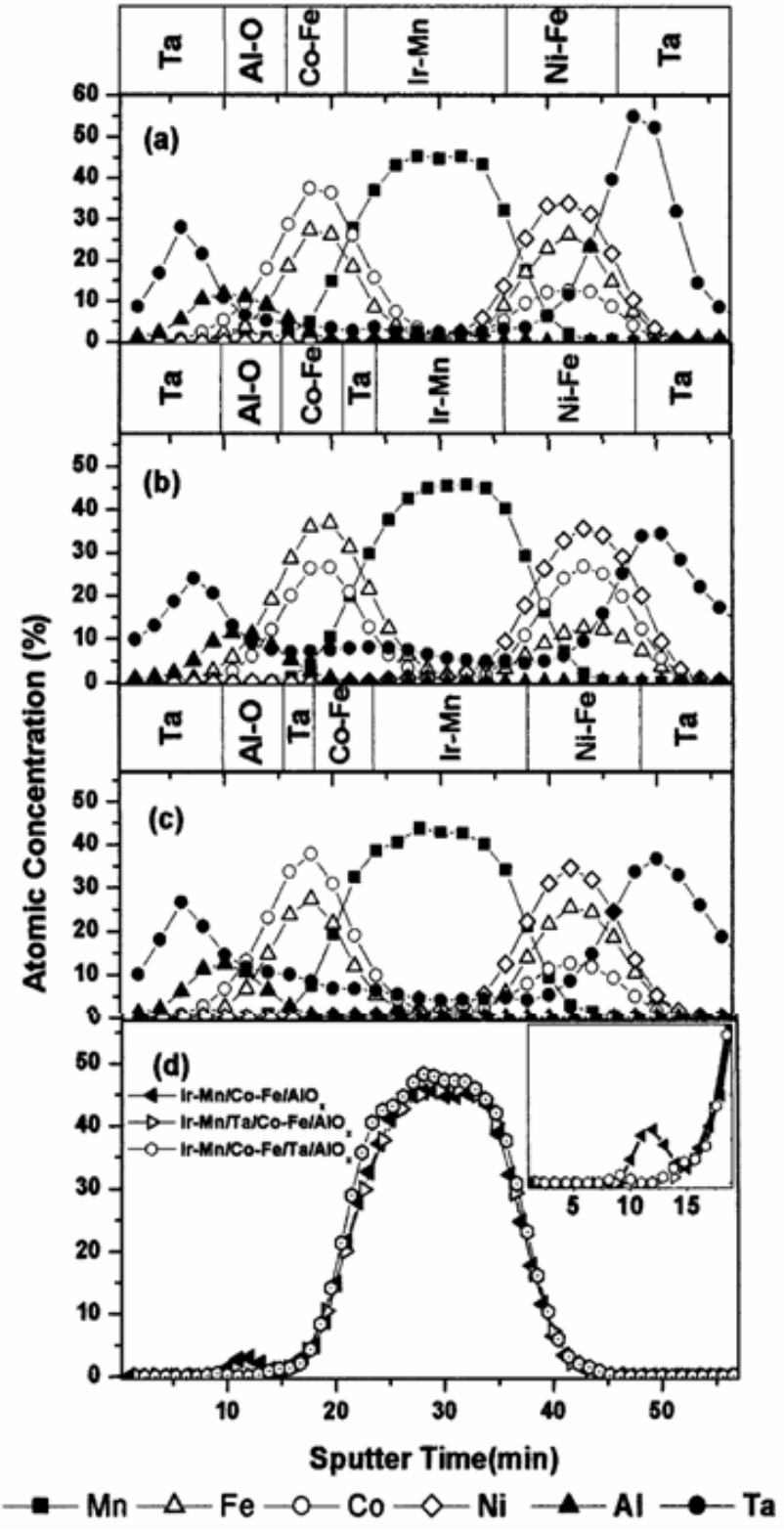

Fig. 2-6 AES depth profiles for (a) IrMn-CoFe-AlOx, (b) IrMn-Ta-CoFe-AlOx, (c) IrMn-CoFe-Ta-AlOx film stacks after annealing at 300°C, and (d) Mn profiles for the three multilayers after annealing at 300°C. (Data are from Ref. [68])

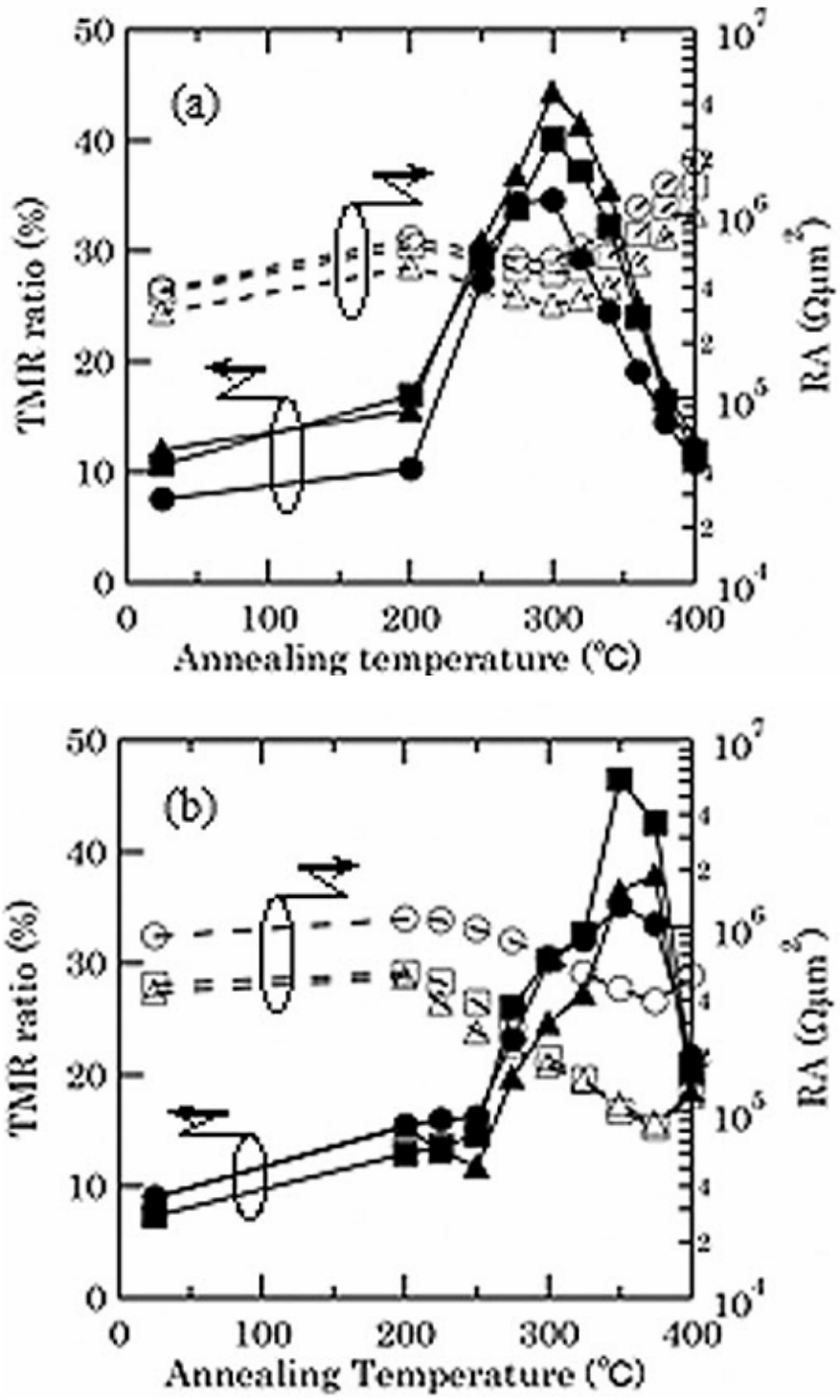

Fig. 2-7 Annealing temperature dependence of TMR ratio and RA for tunnel junctions with (a) CoFe and (b) CoFe/CoFeOx/CoFe pinned layers. ● (○), ▲ (Δ), and ■ (□) represent the data for the junctions prepared under the same conditions, and solid and dashed lines indicate TMR ratio and RA, respectively. (Data are from Ref. [69])

2-4 General properties of Os

Osmium metal is lustrous, bluish white, extremely hard, and brittle even at high temperatures. It has the highest melting point and lowest vapor pressure of the platinum group. The metal is very difficult to fabricate, but the powder can be sintered in a hydrogen atmosphere at a temperature of 2000°C. The solid metal is not affected by air at room temperature, but the powdered or spongy metal slowly gives off osmium tetroxide, which is a powerful oxidising agent and has a strong smell. The tetroxide is highly toxic, and boils at 130°C (760 mm). Concentrations in air as low as 10^{-7} g m^{-3} can cause lung congestion, skin damage, or eye damage. It would not normally be necessary to make a sample of osmium in the laboratory as the metal is available, at a price, commercially. The industrial extraction of osmium is complex as the metal occurs in ores mixed with other metals such as ruthenium, rhodium, palladium, silver, platinum, and gold. Sometimes extraction of the precious metals such as iridium, rhodium, platinum and palladium is the main focus of a particular industrial operation while in other cases it is a byproduct. The extraction is complex because of the other metals present and only worthwhile since osmium is useful as a specialist metal and is the basis of some catalysts in industry. Some other parameters are listed in the Table 2.3 [89].

Table 2.3 General properties of osmium (data are from Ref. [89])

The essentials			
Atomic number	76	Atomic weight	190.23 g
Group number	8	Period number	6
Block	d block	CAS Registry ID	7440-04-2
Brief description			
Standard state	solid at 298 K	Color	bluish grey
Classification	Metallic		
Thermal properties			
Melting point	3033°C	Boiling point	5012 °C
Superconduction temperature	0.66 K		
Conduction properties			
Thermal conductivity	88 $Wm^{-1}K^{-1}$	Coefficient of linear thermal expansion	$5.1*10^{6}\ K^{-1}$
Enthalpies			
Enthalpy of fusion	31 $kJmol^{-1}$	Enthalpy of vaporization	630 $kJ\ mol^{-1}$
Enthalpy of atomization	789 $kJ\ mol^{-1}$		
Bulk properties			
Density of solid	22610 $kg\ m^{-3}$	Molar volume	8.42 cm^{3}
Velocity of sound	4940 $m*s^{-1}$		

TABLE 2.3 General properties of osmium (continued)

Elastic properties				
Rigidity modulus	222 GPa		Poissons ratio	0.25
Hardness				
Mineral hardness	7.0		Brinell hardness	3920 MN m^{-2}
Electrical properties				
Electrical resistivity			8.1 10^{-8} Ω m; or mΩ cm	
Crystal structure				
Space group	P63/mmc		Structure	hcp (hexagonal close-packed)
Cell parameters	a	273.44 pm	α	90°
	b	273.44 pm	β	90°
	c	431.73 pm	γ	120°
Electronic properties				
Electron affinity	106.1 kJ mol^{-1}		Atomic radius (empirical)	130 pm
Atomic radius (calculated)	185 pm		Covalent radius (empirical)	128 pm

2-4-1 Previous experiments and reports of uses of Os

Compressibility (reciprocal of the bulk modulus) is an important physical property of a material, providing useful information about material strength, chemical bonding, and electronic structure. H. Cynn et al. reported that metallic osmium had a lower compressibility than covalently bonded diamond [90]. By fitting the compression data with third-order Birch-Murnaghan equation of state (EOS), the volume compressions for some transition metal was shown in the Fig. 2-8. It is notable that the P-V/V_0 curve for diamond is lower than the EOS fit for Os at high pressure. The fitted results also showed that the experimentally determined bulk modulus for Os at ambient conditions is 462 GPa, even greater than the value of 443 GPa for diamond. Such high hardness of osmium has led to its alloy use for the gramophone record styli and electric light filaments (Osram) in the past [91]. Furthermore, Due to its higher reflectance, osmium has also been found to be useful as an optical coating for far-UV instruments and to be attractive in the application of the overcoating on the Space Shuttle [92]. However, the application of Os in integrated circuits industry was rare in 1970s.

The epitaxial metal silicides have attracted much attention for their potential applications in the integrated circuits industry and for a critical understanding of the feature of the silicide/Si system corrected with the important properties such as sheet resistivity and Schottky barrier height [93-94]. The reactions of osmium thin film with their silicon substrates lead to the formation of the Os_2Si_3 and $OsSi_2$ phases were reported by C. S. Peterson et al [95]. They found the Os films similarly deposited would fail by peeling during subsequent heat treatment. Sufficient adhesion could be obtained only by limiting the thickness to 300 Å, and with substrate temperature preferably raised to 400°C. Thus, a 500 Å-thick ruthenium layer was used for improving the adhesion of the Os film prepared by an e-bam evaporation system. Annealing at about 500°C led to the formation of Os_2Si_3, whereas

the silicon rich phase, $OsSi_2$, occurred after 750°C, as shown in Fig 2-9. Besides, the epitaxy osmium silicide was reached by electroless plating and heat treatment was also suggested by Y. S. Chang et al [96]. The etched wafers were immersed into a special osmium hypophosphite-based electroless plating bath for a few minutes to deposit an osmium thin film autocatalytically at 85°C with the pH value of the bath was maintained at 10. A two-step annealing scheme with the first step at a temperature of 200°C, follow by a second step at 1000°C, was found to be effective in promoting epitaxial growth. As shown in Fig. 2-10, the orientation relationship between $OsSi_2$ and Si were analyzed to be [10$\underline{2}$] $OsSi_2$ // [111] Si and (040) OsSi2 // (2$\underline{2}$0) Si.

The sputtered γ-Fe_3O_4 thin film was suggested to be a high density magnetic media material due to its low media noise in 1980s. O. Ishii et al. reported that Os was added into Fe_3O_4 thin film for obtaining both higher H_c and higher S* than in previously reported material, Co, Ti, and Cu. The coercivity and coercive squareness of the film increase with Os content [97]. A γ-$(Fe_{0.948}Os_{0.052})_2O_3$ film showed the maximum coercivity of 2100 Oe and high coercive squareness of 0.81 as shown in Fig. 2-11. Except the rising of the H_c and the S*, the Os doping also brought out magnetic field-induced anisotropy after field annealing. A field-induced anisotropy of 10^5 erg/cc was resulted from the γ-Fe_2O_3 thin film after 250°C annealing for 1 hr during a 7 kOe of external field. In 1987, they also presented that the average grain size of sputtered γ-Fe_2O_3 thin film was markedly decreased by Os addition [98]. The grain size of γ-Fe_2O_3 films decreases from 84 to 35 nm as the Os content increases from 0 to over 0.88 at.%. According to the refining effect, the reducing reaction brings about an increase in the saturation magnetization and in the squareness ratio of γ-Fe_2O_3 thin film (as seen from Fig. 2-12). Such an Os-added γ-Fe_2O_3 thin film disk has higher output voltage and SNR than other disks.

Cu interconnects was suggested to replace Al-based one in ultra-large scale integration device for improving the electrical properties. The advantages of Cu to be good interconnects are their low resistance and their high electromigration resistance resulted its high melting point. The main electromigration paths of Cu interconnect are the interface between Cu and the dielectric capping layer and that between Cu and the diffusion barrier. H. Kim et al. [99] reported that Os was selected as the one of the best glue layers due to the reasons as follows. First, Os did not dissolve at process temperature and did not form any intermetallic compounds with Cu. Second, Os has a relative low resistivity between the transition metals except the Cu, Ag, and Au. Third, Os has relative high melting point to prevent the agglomeration of a glue layer during the process. Of fourth, Os also strongly adhere to Cu, as seen from Table 2.4. Thus, Kim et al. did agree Os has a high potential for use as a glue layer or a new barrier layer of ULSI Cu interconnects process. On the other hand, D. Josell et al. [14] investigated that osmium was as a diffusion barrier for the seedless Cu electrodeposition superfilling of sub-micrometer trenched. They mentioned that Os exhibits electronic, chemical, and metallurgical properties that are quite similar to those of Ru. Os could be suggested to superior to Ru as a diffusion barrier because of the reasons as listed following: 1) Os has a bulk electrical resistivity that nearly as low as that of Ru (well below that of Ta significantly); 2) Os, like Ru, has extremely low mutual solubility with Cu; and 3) the melting point is ~700 K higher than that of Ru, exceeding even that of Ta (seen from Table 2.5). These data demonstrated that Os barrier, like Ru, permit copper wetting and superfill of Damascene trenched by direct electrodeposition. Figure 2-13 shows the results of filling of trenches with five different widths for deposition times ranging from 5 ~ 20 s. They also reported that Os/Cu system might be of interest for Damascene interconnects applications though the Os's effective thickness as a diffusion barrier remains to be established.

Table 2.4 Wetting angle of Cu on glue layers and calculated energy of Cu adhesion to glue layers (Data are from Ref. [99])

Element	Ta	Mo	Ru	Os
Wetting angle (°)	123	61	43	50
Relative adhesion energy (γ_{Cu})	0.46	1.48	1.73	1.64

Table 2.5 Melting temperature and transport properties for Ta and the selected potential replacement materials (Data are from Ref. [14])

	Melting temperature (K)	Electrical resistivity ($\mu\Omega$ cm)	Thermal conductivity [W/(m K)]
Osmium	3306	8.1	88
Ruthenium	2607	7.1	120
Tantalum	3290	13	57

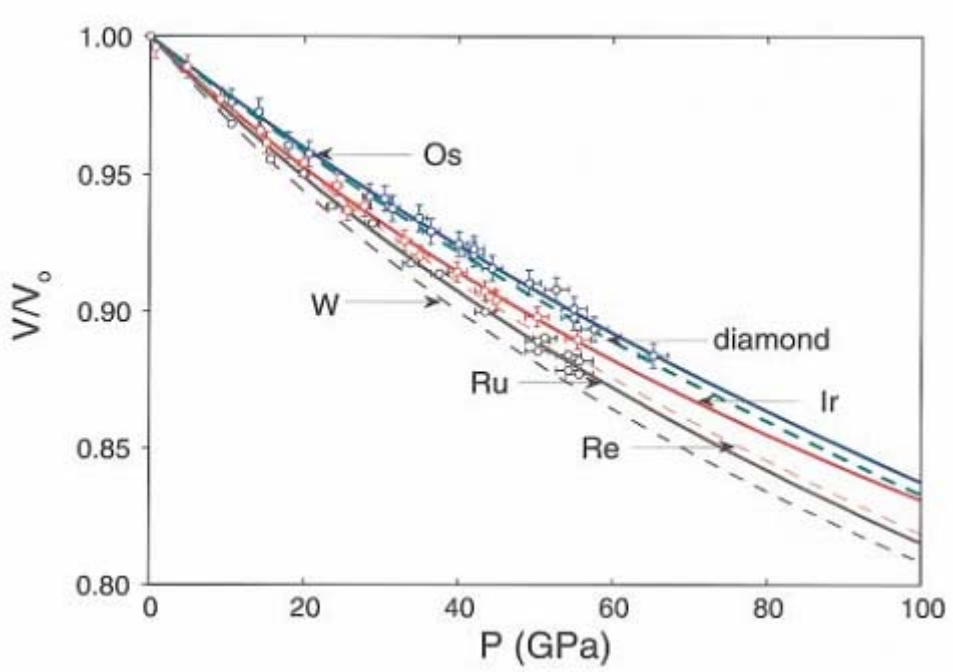

Fig. 2-8 Volume compressions for Os, Ir, Re, Ru, W, and C. Error bars are shown for Os, Ir, and Ru. (Data are from Ref. [90])

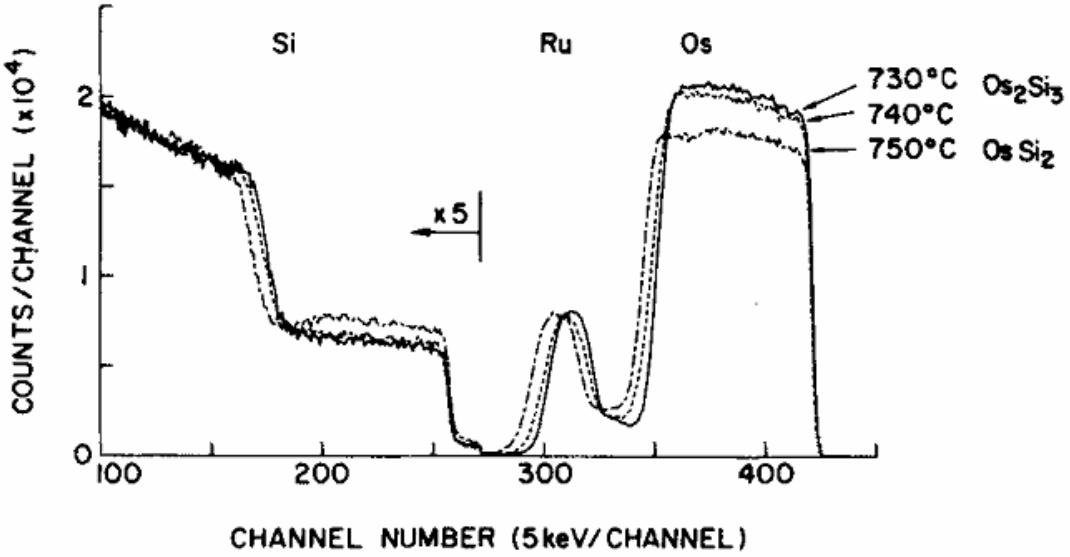

Fig. 2-9 Backscattering spectra for osmium samples heat treated for one hour at 730, 740, and 750°C, respectively, showing the transition from Os_2Si_3 to $OsSi_2$. (Data are from Ref. [95])

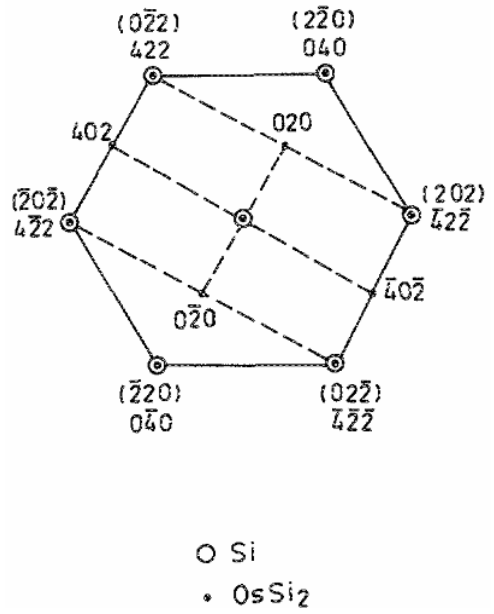

Fig. 2-10 The indexed pattern of overlapping (040) $OsSi_2$ // (2$\underline{2}$0) Si and [10$\underline{2}$] $OsSi_2$ // [111] Si, after 200-1000°C, two-step annealing. (Data are from Ref. [96])

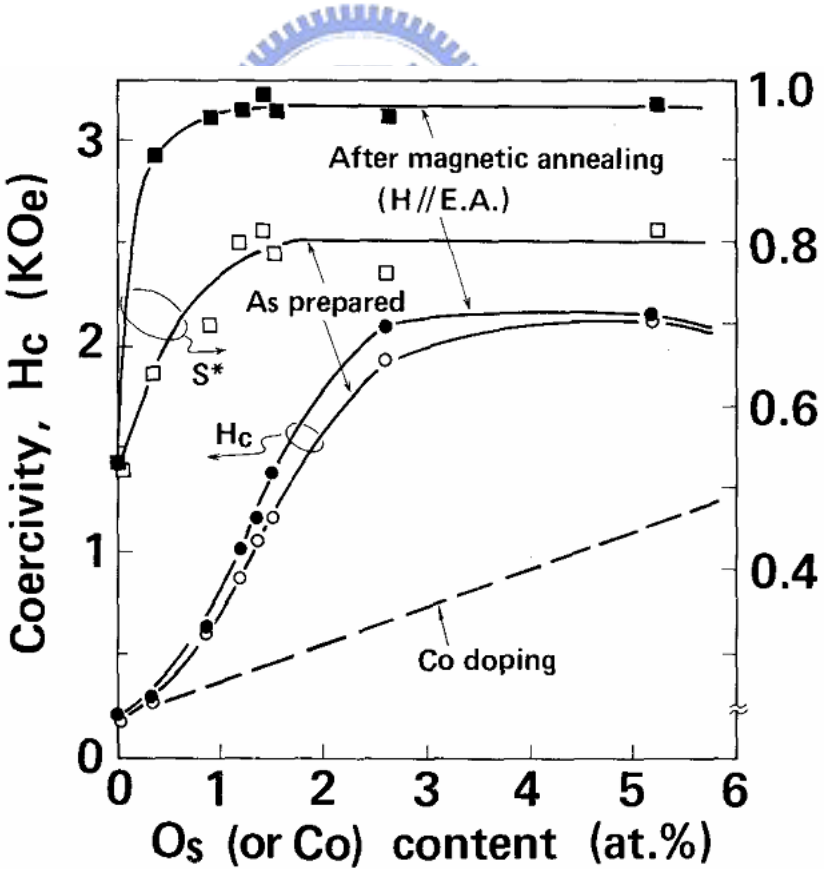

Fig. 2-11 Coercivity H_c and coercive squareness S* before (○:H_c, □: S*) and after (●:H_c, ■: S*) magnetic annealing as a function of Os constant. (Data are from Ref. [97])

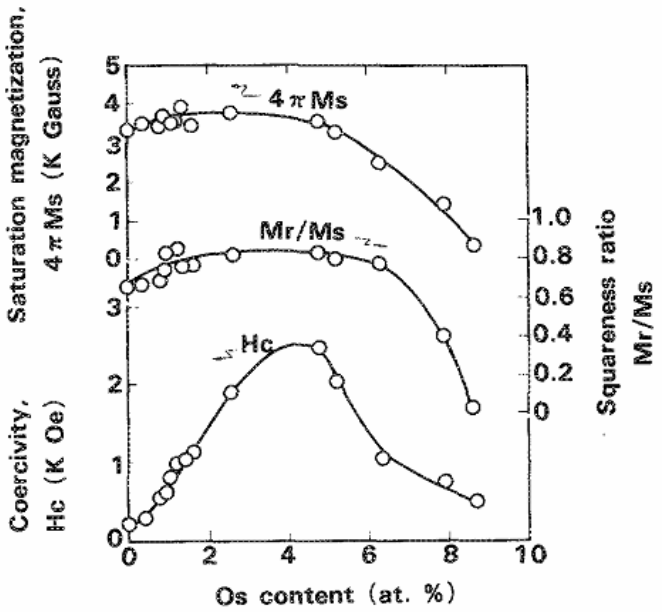

Fig. 2-12 Relation between Os content and the magnetic properties of γ–Fe_2O_3 thin films. The reduction temperatures of pure and Os-added films were 300 and 250°C, respectively. (Data are from Ref. [98])

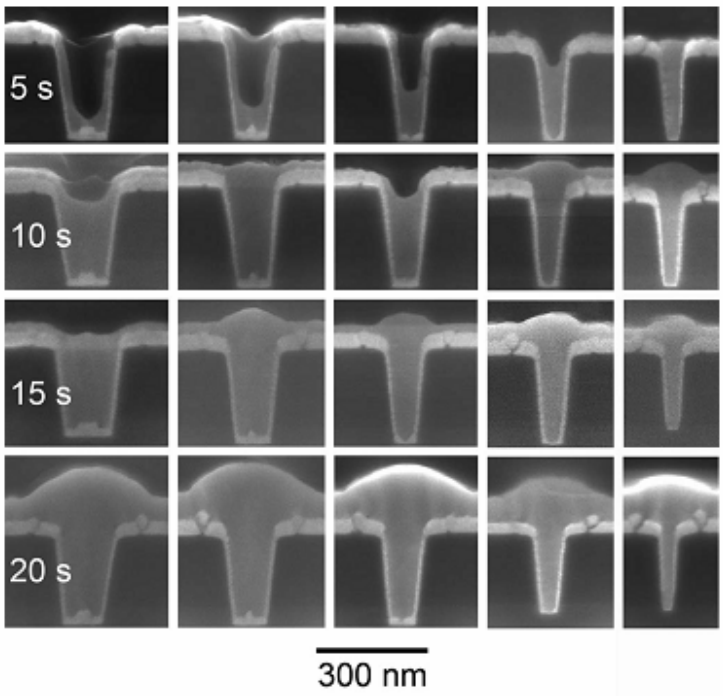

Fig.2-13 Cross-sectional SEM images of Cu electrodeposited directly in trenches of various aspect ratios. The Os barrier upon which the Cu was electrodeposited is visible as a bright layer beneath the Cu. (Images are from Ref. [14])